

Electrocatalysis

Self-Supported Nanoporous Au₃Cu Electrode with Enriched Gold on Surface for Efficient Electrochemical Reduction of CO₂Xiaoming Ma,^[a] Yongli Shen,^[a] Shuang Yao,^{*,[a]} Miao Shu,^[b] Rui Si,^{*,[b]} and Changhua An^{*,[a]}

Abstract: The key to the electrochemical conversion of CO₂ lies in the development of efficient electrocatalysts with ease of operation, good conductivity, and rich active sites that fulfil the desired reaction direction and selectivity. Herein, an oxidative etching of Au₂₀Cu₈₀ alloy is used for the synthesis of a nanoporous Au₃Cu alloy, representing a facile strategy for tuning the surface electronic properties and altering the adsorption behavior of the intermediates. HRTEM, XPS, and EXAFS results reveal that the curved surface of the synthesized nanoporous Au₃Cu is rich in gold with unsaturated coordination conditions. It can be used directly as a self-supported electrode for CO₂ reduction, and exhibits

high Faradaic efficiency (FE) of 98.12% toward CO at a potential of -0.7 V versus the reversible hydrogen electrode (RHE). The FE is 1.47 times that over the as-made single nanoporous Au. Density functional theory reveals that *CO has a relatively long distance on the surface of nanoporous Au₃Cu, making desorption of CO easier and avoiding CO poisoning. The Hirshfeld charge distribution shows that the Au atoms have a negative charge and the Cu atoms exhibit a positive charge, which separately bond to the C atom and O atom in the *COOH intermediate through a bidentate mode. This affords the lowest *COOH adsorption free energy and low desorption energy for CO molecules.

Introduction

Electrocatalysts are at the heart of the design of efficient electrochemical systems with the ability to decrease kinetic activation barriers and boost reaction efficiency.^[1] Great strides have been made in the development of active electrocatalysts, including decreasing the size to increase surface area,^[2] and engineering the composition and shape to improve the intrinsic activity of the active sites,^[3] so as to manipulate the transportation of reactants and products on the electrolyte/electrode interface.^[4] A popular way to fabricate electrodes is to deposit corresponding nanoparticles onto a conductive support.^[5] Associated issues such as the loss or aggregation of catalysts often occur, especially during long-term reactions.^[6] On the

other hand, the complexity in the system increases the challenge of understanding the kinetic process and ascertaining the origin of the surface catalytic activity. The development of an integrated electrode with good conductivity, high activity, and ease of surface engineering is highly desirable for the fundamental understanding and design of efficient electrocatalytic systems.

Three-dimensional nanoporous metals have the merits of intrinsic conductivity and fruitful nanoscale interconnected ligaments and channels.^[7] These beneficial micro/nanostructures facilitate intermediate mass/electron transport, making them a class of promising electrocatalysts toward the CO₂ reduction reaction (CO₂ RR),^[8] which is attractive for mitigating warming gas emissions and realizing resource utilization. The CO₂ RR products can either be liquid fuels (e.g., ethanol) or gaseous products such as CO for thermocatalytic transformations.^[9] To date, the CO₂ RR has not been a widespread technology because of the low energy efficiency and high overpotentials required, a lack of electrocatalytic stability, and unsatisfactory selectivity.^[10] Noble metals such as Au/Ag have been essential for the electrochemical CO₂ RR to CO.^[5,11] However, the high cost and low earth abundance hampers their application. Various strategies, from controlling the size to tailoring the exposed facets, and surface functionalization with molecular decorations, have been developed to improve their performances.^[12] A class of nanoporous Ag electrodes from Jiao's group with intrinsic curved surfaces is capable of reducing CO₂ to CO with a 92% Faradaic efficiency (FE) and a relatively high current density of 18 mA cm⁻² at -0.6 V (vs. RHE).^[10a] Zhang et al. reported that low-coordinated gold atoms are responsible for the enhanced electrocatalytic CO₂ RR over porous Au.^[13] However,

[a] X. M. Ma, Dr. Y. L. Shen, Dr. S. Yao, Prof. C. An
Tianjin Key Laboratory of Organic Solar Cells and
Photochemical Conversion, School of Chemistry and
Chemical Engineering and Tianjin Key Laboratory of
Advanced Functional Porous Materials, Institute for
New Energy Materials & Low-Carbon Technologies
Tianjin University of Technology, Tianjin 300384 (China)
E-mail: shuangyao@email.tjut.edu.cn
anch@tjut.edu.cn

[b] M. Shu, Prof. R. Si
Shanghai Synchrotron Radiation Facility
Shanghai Institute of Applied Physics, Chinese Academy of Sciences
Shanghai, 201204 (China)
E-mail: sirui@sinap.ac.cn

 Supporting information and the ORCID identification number(s) for the author(s) of this article can be found under:
<https://doi.org/10.1002/chem.201904619>.

 Part of a Special Issue on Electrocatalysis: Mechanism and Applications. To view the complete issue, visit Issue 18, 2020.

tuning of the selectivity and the suppression of side reactions of hydrogen evolution with a single catalyst is still a challenge because of the multistep nature and complexity of the CO₂ RR. Alloying cost-effective Cu with the capacity to convert CO₂ into useful chemical substances is a promising strategy in which the composition and electronic properties of the alloy surface can be finely tuned to alter the reaction intermediate adsorption behavior.^[14] The development of bimetallic AuCu-based catalysts to break the scaling relationship and stabilize the reaction intermediates to lower the overpotential is beneficial for enhancing the reaction activity, selectivity, and stability.^[15] Open questions still remain regarding the synthesis and scale-up of nanoporous alloys with controlled composition and targeted surface catalytic sites. In addition, large void volumes (>70%) mean they have poor mechanical properties, limiting their practical implementation.

In this work, we have achieved synthesis of self-supported nanoporous Au₃Cu with gold-enriched surface through the controlled oxidative etching of Au₂₀Cu₈₀ alloy under mild conditions. The good conductivity and flexibility of the as-prepared nanoporous Au₃Cu allow it to be used directly as a self-supported efficient electrode, which is capable of reducing CO₂ to CO with a Faradic efficiency (FE) as high as 98.12% with a current density of 12.77 mAcm⁻² at a low potential of -0.7 V versus RHE. The value is even higher than the reported value^[13] and over self-made nanoporous gold under similar conditions, implying that the use of Cu not only reduces the cost, but also improves the reaction selectivity toward CO. Furthermore, it can maintain a high FE of CO in a broad potential. Density functional theory reveals that the nanoporous Au₃Cu has the lowest *COOH adsorption energy, and a decreased energy required for CO desorption. The introduction of Cu makes the Au atom surface more negatively charged than the single nanoporous Au, forming a stable double-dentate structure for the *CO adsorption on the surface of porous Au₃Cu with a relatively long distance, leading to the easier desorption of CO. This work presents a convenient approach for tuning

the surface engineering of self-supported nanoporous alloys with promising applications in the fields of new energy and environmental catalysis.

Results and Discussion

Figure 1 a shows the XRD pattern of the as-prepared nanoporous Au₃Cu. The diffraction peaks at 38.1°, 44.25°, 64.33°, 77.55°, and 81.50° can be assigned to the (111), (200), (220), (311), and (222) planes of the face-centered cubic (FCC) structure, respectively, demonstrating the successful synthesis of Au₃Cu. The SEM image (Figure 1 b) clearly reveals its 3D bicontinuous nanoporous nature. The magnified image in the inset of Figure 1 b indicates the ligament and the pore sizes of approximately 50 nm. For comparison, as seen from Figure S2 (Supporting Information), both nanoporous Au and Cu are also in the FCC phase. A thin oxide shell is found on the nanoporous Cu because of its inevitable oxidation in air.^[5b] Figure S3 a (Supporting Information) shows that the nanoporous Au has the same structure as the Au₃Cu. For nanoporous Cu, Figure S3 b reveals quasi-2D nanoporous arrays, possessing 3D networks in the microcosm. The thickness of the nanosheets and the ligament size are approximately 40 and 30 nm, respectively.

As shown in Figure 1 c, most ligaments possess positive, negative, and saddle-like surface curvatures, which are different from the nanoparticles with relatively well-defined shape and only convex surface curvature at the corners.^[16] Furthermore, the interplanar distances from the adjacent lattice fringes in the HRTEM images (Figure 1 d) are about 0.24, 0.21, and 0.124 nm, corresponding to the (111), (200), and (311) planes of FCC Au₃Cu, respectively. EDX elemental mapping (Figure 1 e–h) shows that Au and Cu are distributed over the entire ligament. The integration diagram shows that the surface gold content is higher than the bulk average content. The linear scan elemental map (Figure 1 i) reveals that the gold signals on both sides are stronger than the central region, whereas the reverse

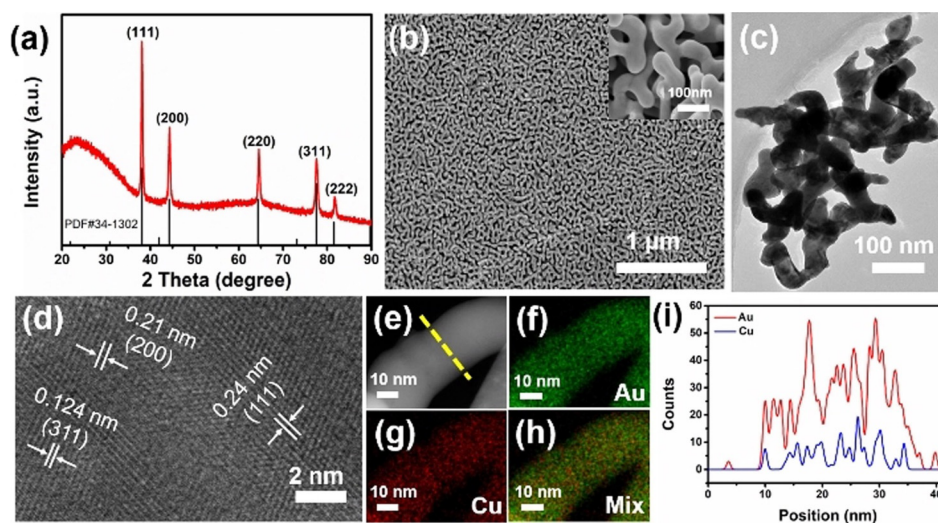


Figure 1. a) XRD pattern of the as-prepared Au₃Cu alloy. b) Low- and high-magnification SEM images of nanoporous Au₃Cu. c, d) HRTEM image, e–h) STEM-EDS elemental mapping of Au₃Cu, and i) line profiles of Au and Cu recorded along the dashed line shown in e).

signals occur over Cu, implying the Au₃Cu surface is enriched in gold.

XPS was applied to characterize the surface composition and oxidation state of nanoporous Au₃Cu in detail. Figure 2a and b show the high-resolution spectra of the Au 4f and Cu 2p regions over Au₃Cu. The Au 4f spectrum exhibits binding

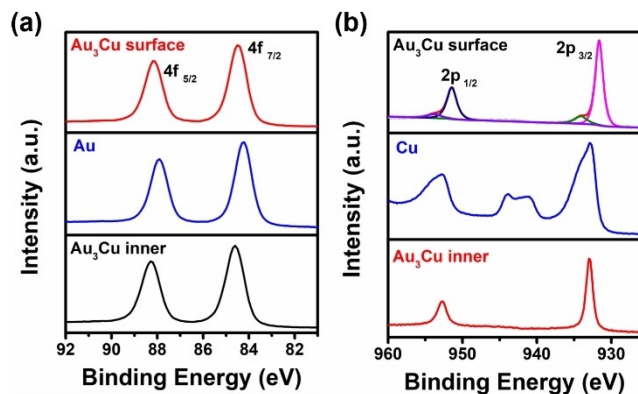


Figure 2. XPS spectra of a) the Au 4f region and b) the Cu 2p region.

energy (B.E.) peaks of 4f_{7/2} and 4f_{5/2} at 84.5 and 88.2 eV, respectively, coinciding with the state of metallic Au. The band positions have a slight shift toward higher energy compared with pure nanoporous Au because of the electronic interaction between Au and Cu in the alloy. The surface Au content is 77.95%, confirming that gold is rich on the surface. In the Cu 2p region, the peaks at 932.7 and 952.6 eV are assigned to the binding energies of Cu 2p_{3/2} and Cu 2p_{1/2}, respectively, indicating the existence of Cu⁰. In addition, the remaining small peaks at 934.48 and 953.78 eV can be assigned to CuO, which comes from the inevitable oxidation of the sample in air.^[17] In comparison with pure nanoporous Cu, the band positions have a significant negative shift, demonstrating that the surface copper (content of 22.05%) has a little bonding with the surface gold.^[12b] For the cross-section, the ratio of Au is decreased to 72.88%, which is lower than that on the surface. The B.E. values of Au 4f_{7/2} and 4f_{5/2} shift to higher energy compared with those for single nanoporous Au. Correspondingly, the B.E. values of Cu 2p_{3/2} and Cu 2p_{1/2} move to the opposite direction. It is reasonable to infer that the valence electrons transfer from the Cu atom to the Au atom owing to their discrepancy of electronic negativities, resulting in the redistribution of interatomic charges. A decrease in B.E. over the Cu atom reflects the downshift of the d-band center, weakening the chemisorption of oxygen-containing species such as CO_{ads} and OH_{ads} on the surface.^[5a,18]

To gain insights into the surface coordination environments of the nanoporous Au₃Cu, we collected the XANES spectra from Au₃Cu at the Au L₃ edge. As shown in Figure 3a, the edge positions of Au in the XANES profile of Au₃Cu have a similar edge shape to that of the reference Au foil, indicating its full Au⁰ state.^[19] Additionally, it has a small increase in intensity above the Au foil in the region from 11 920 to 11 950 eV. This region is where the “white line” absorption occurs, indicating

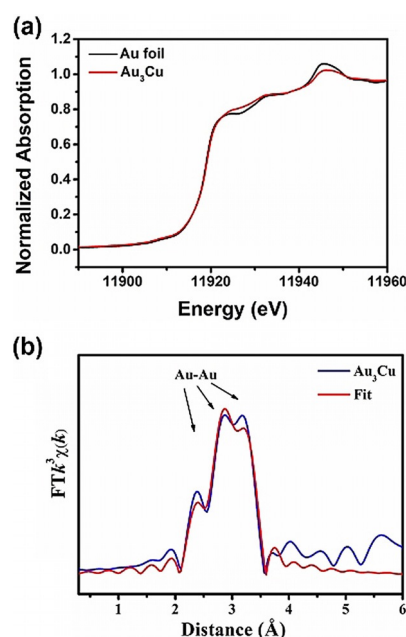


Figure 3. X-ray fine absorption spectra of Au₃Cu. a) XANES spectra, b) EXAFS spectra at the Au L₃-edge.

increased electron density over the d-band of Au. The magnitude of the change in the white line is consistent with those over bulk AuCu alloys.^[20] The edge position has a slight shift toward high photon energies compared with Au foil. The phenomena at the two edges are caused by the electron transfer from Cu to Au, which is consistent with the XPS analyses. The loss of electrons in the Cu d-band is compensated by gaining s-p bands.^[21] The EXAFS experiments with data fitting in *R* space were performed to determine the short-range local coordination structure, including distances (*R*) and coordination numbers (*CN*) around the gold atoms. As revealed in Figure 3b and Table S1 (Supporting Information), three peaks in the range 2.2–3.5 Å can be assigned to the contribution from metallic Au-Au with a *CN* number of 7.3. Figure S4 (Supporting Information) presents EXAFS data of nanoporous Au₃Cu, showing the coordination environment surrounding Au and Cu. The Au L₃-edge of nanoporous Au₃Cu exhibits a larger first-shell scattering amplitude, which can be attributed to the stronger constructive interference of photoelectron scattering. The lower *CN* for gold indicates that the Au atoms are relatively unsaturated compared with Cu, resulting from the gold enrichment at the surface.

The as-synthesized nanoporous Au₃Cu can be applied directly as an electrode for the CO₂ RR. Figure 4a shows the linear sweep voltammetry (LSV) curves in the N₂ and CO₂ atmosphere over nanoporous Au, Cu, and Au₃Cu, respectively. The applied potential was in the range from 0 to –1.4 V (vs. RHE) at a sweep rate of 50 mV s^{–1}. Significant differences were observed among the LSV curves of Au, Cu, and Au₃Cu between the N₂ and CO₂-saturated electrolytes. The total current densities (reaction activities) increased significantly in the CO₂-saturated electrolyte, showing an apparent contribution of the CO₂ RR to the whole reaction. The activity of nanoporous Au₃Cu was sig-

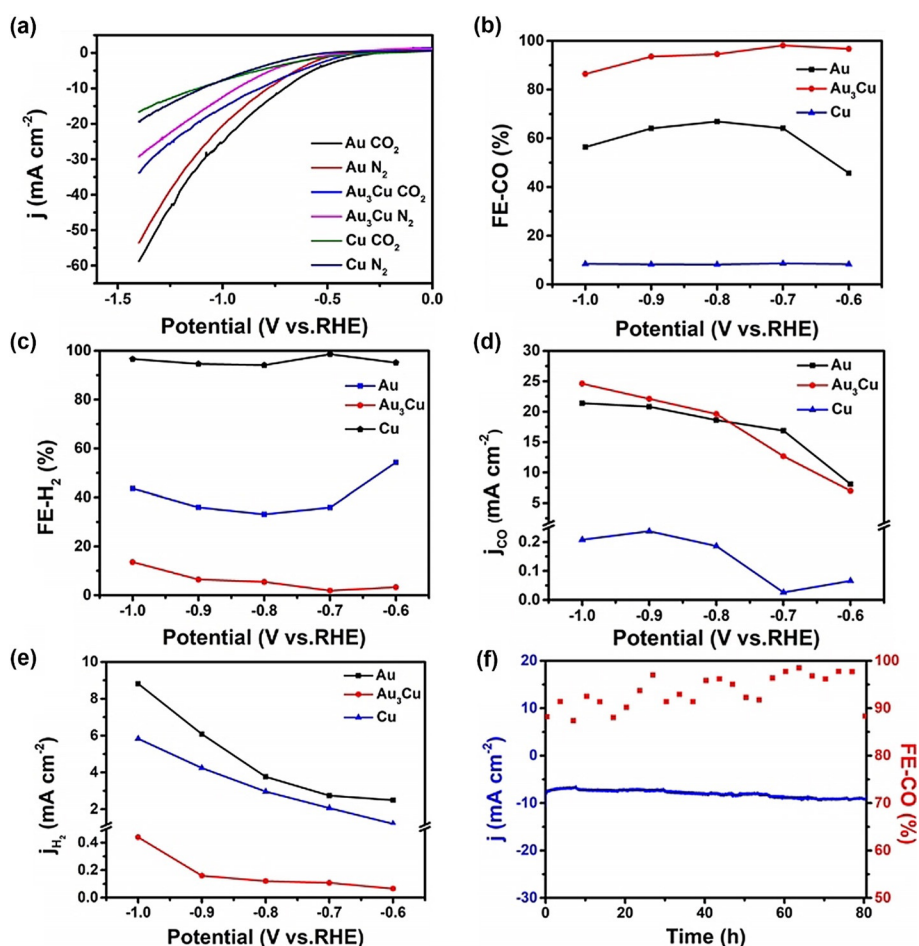


Figure 4. Electrocatalytic CO₂RR performance of Au, Au₃Cu, and Cu. a) LSV in N₂- and CO₂-saturated 0.1 M KHCO₃. b,c) FE of CO and H₂ under different applied potentials. d,e) Partial current of CO and H₂ production at various potentials. f) CO₂RR stability test of the current density on self-supported Au₃Cu nanoporous electrode at -0.7 V versus RHE for 80 h.

nificantly higher than that of single nanoporous Cu. Although it is somewhat lower than that of nanoporous Au, the HER gradually dictates the ability of nanoporous Au with the increase in potential. Thereafter, stepped-potential tests were conducted from -0.6 to -1.0 V (vs. RHE). As shown in Figure 4b,c, CO and H₂ are the major products, with the total FE approaching 100%. Note that the selectivity of nanoporous Cu is poor, and the FE of CO is rather low, and does not increase with the change in potential. The nanoporous Au is affected significantly by the potential. As the potential increases, the HER becomes more serious. However, in the case of nanoporous Au₃Cu, as the potential becomes more negative, the FE of CO increases and the HER is suppressed.

The CO₂-to-CO conversion was initiated from -0.6 V versus RHE, rapidly increased to a conversion ratio of 96.73%, and reached the highest FE of 98.12% at -0.7 V versus RHE. The FE value is 1.47 times that over pure nanoporous Au. The selectivity is also higher than the reported data over AuCu alloys.^[22] Moreover, a high FE of CO can be maintained over a wide range of applied potentials. The potential required at the highest FE is much lower than that for nanoporous Au. Figure 4d,e compares the partial current densities of CO and H₂. It can be seen that the partial current density for CO production would

be increased remarkably along with the increase in applied negative potential, indicating that the reaction rate of the CO₂ RR is accelerated at high potentials.^[23] Meanwhile, the partial current density of CO over nanoporous Au₃Cu is much higher than that over Cu. Owing to the high HER at high potentials, the CO partial current density of nanoporous Au is lower than that of Au₃Cu. As shown in Figure 4e, the sub-current density of H₂ over Au at the same overpotential is about 20 times higher than that over Au₃Cu (≈ 0.44 mA cm⁻² at -1 V vs. RHE), further demonstrating the high activity and selectivity of Au₃Cu toward the CO₂ RR. Figure 4f shows that the total current density over nanoporous Au₃Cu is still maintained at around 10 mA cm⁻² after electrolysis for more than 80 h at a potential of -0.7 V. The XRD results (Figure S5, Supporting Information) show that the pattern did not change and remained as Au₃Cu. The SEM image in Figure S6 (Supporting Information) shows that the nanoporous structures is still retained. The mapping and XPS (Figures S7 and S8, Supporting Information) show that the surface is still rich in the Au structure, and no significant change is observed, suggesting its good stability. For nanoporous Au, after testing under the same conditions, the current density and the FE of CO decreased after 50 h because of the vigorous surface HER (Fig-

ures S9 and S10 Supporting Information), although the porous structures showed no change. The nanoporous Cu can only be maintained for about 7.5 h at -1.0 V versus RHE, (Figure S11, Supporting Information) which is significantly lower than that of the nanoporous Au_3Cu , and the porous structure is completely collapsed (Figure S12).

For comparison, solid Au_3Cu was also obtained by annealing nanoporous Au_3Cu alloys at 500°C . The XRD pattern in Figure S13 (Supporting Information) indicates that the constituents of the obtained solid Au_3Cu are basically the same as those of the porous sample. The pores disappeared after annealing, and the selectivity toward the CO_2 RR is apparently decreased (Figures S14 and S15). Therefore, the nanoporous Au_3Cu with unsaturated coordination Au atoms and curved interfaces plays an essential role in the enhancement of the CO_2 RR performance.

The most important elementary process in the preparation of CO through the CO_2 RR is the formation of $^*\text{COOH}$ intermediates and the subsequent dissociation of $^*\text{CO}$. Figure 5a plots the formation energy of $^*\text{COOH}$ and adsorption energy of $^*\text{CO}$. The lower the ordinates, the smaller the free energy change to be overcome for the generation of $^*\text{COOH}$ intermediates on the catalyst surface. The more positive the adsorption free energy of $^*\text{CO}$ adsorption on the catalyst, the easier the dissociation of $^*\text{CO}$ from the surface, which is beneficial for the completion of the entire reaction. Among all the catalysts examined, the nanoporous Au_3Cu {311} has the lowest free energy change of $^*\text{COOH}$ formation, and the energy required for $^*\text{CO}$ desorption is relatively low. Therefore, Au_3Cu {311} has the best catalytic activity. The average distance between $^*\text{CO}$ and the surface in Figure 5b also indicates that there is a relatively long distance between $^*\text{CO}$ and Au_3Cu {311} in the adsorption structure, facilitating $^*\text{CO}$ desorption. Therefore, the catalyst is not prone to be poisoned by CO. The Hirshfeld charge distributions of Au_3Cu {311} and Au {311} in Figure 5c,d show that the surface of pure Au is negatively charged, so it prefers to interact with positively charged C atoms in the $^*\text{COOH}$ intermediate, whereas the surface $\text{Au}^{\delta-}$ has a repulsion effect on the negatively charged O atoms in

$^*\text{COOH}$. Therefore, the $^*\text{COOH}$ intermediate tends to be a monodentate form on single Au (Figure 5c). The introduction of Cu to Au changes the surface charge distribution of the catalyst significantly. Electronic charge redistributed from Cu to Au creates regions of localized positive charge on the Cu sites, whereas the Au atoms around the Cu atoms are clearly more negatively charged. This positive and negative charge center can be bonded simultaneously with the C and O atoms in the $^*\text{COOH}$, forming a more stable (lower energy) bidentate adsorption structure (Figure 5d). Therefore, the formation of $^*\text{COOH}$ becomes easier on the surface of Au_3Cu , and boosts CO production.

Conclusions

In summary, we have developed a mild oxidative etching route for the synthesis of 3D nanoporous Au_3Cu with enriched gold on the surface. The as-obtained nanoporous Au_3Cu can be applied directly as a self-supported electrode for conversion from CO_2 to CO with high efficiency, which is superior to single porous Au and Cu. The nanoporous Au_3Cu realized a high FE_{CO} of 98.12% with a stable current density of 12.77 mA cm^{-2} at a voltage of -0.7 V. The increased catalytic activity is attributed to the presence of a large number of unsaturated coordination active sites on the nanoporous surface, which also promotes transport of the reactants as well as the products. Theoretical simulation reveals that the nanoporous Au_3Cu catalyst has the lowest $^*\text{COOH}$ intermediate adsorption energy, because the introduction of Cu causes more negative charge on the surface of the Au atom, thereby forming a stable double-dentate adsorption mode. Furthermore, $^*\text{CO}$ exhibits a relatively long distance from the surface of nanoporous Au_3Cu , making it easier for CO to desorb from the surface and avoiding CO poisoning. In short, the present work provides a pathway for engineering the phases and surfaces of the nanoporous catalysts.

Experimental Section

Materials synthesis

$\text{Au}_{20}\text{Cu}_{80}$ alloy was prepared in an arc melting furnace (WK type, Physcience Opto-electronics Co., Ltd., Beijing). In a typical procedure, pure metals of Cu (99.99 wt%) and Au (99.99 wt%) were melted three times on a water-cooled copper hearth under a Ti-gettered argon atmosphere. With melt spinning equipment (WK-IIB type, Physcience Opto-electronics Co., Ltd., Beijing), the pre-alloyed ingot was remelted in a quartz tube by high-frequency induction heating. Then, the melt was injected onto a copper roller of 25 cm in diameter, which was rotated at a speed of ≈ 3000 rpm in a controlled argon atmosphere. The as-spun ribbons were $\approx 25 \mu\text{m}$ in thickness, 2.0 mm in width, and 10 cm in length (Figure S1).

Preparation of nanoporous Au_3Cu alloy

The as-prepared $\text{Au}_{20}\text{Cu}_{80}$ (40 mg) was immersed in FeCl_3 solution (0.08 M) at room temperature under stirring for 30 min. Then, the obtained sample was rinsed several times with deionized water, and dried in a vacuum oven at 60°C for 12 h.

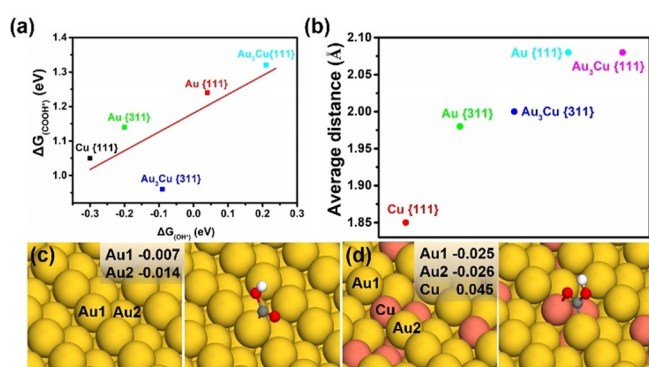


Figure 5. Fitting graph of linear relation between formation free energy of $^*\text{COOH}$ and adsorption free energy of $^*\text{CO}$. a) Average distance between $^*\text{CO}$ and the catalyst surface; b) Hirshfeld charge distribution of Au_3Cu {311} and Au {311} and c,d) $^*\text{COOH}$ adsorption structure on Au_3Cu {311} and Au {311}.

Upon increasing the FeCl₃ concentration to 0.5 M, the nanoporous Au was obtained and the other conditions were kept constant. For comparison, nanoporous Cu was prepared through chemical corrosion of Cu₁₇Al₈₃ ribbons (1.48 g) in alkaline (2 M NaOH) solution for 4 h at 298 K.

Characterizations

X-ray diffraction (XRD, Rigaku UltimaIV) was performed to analyze the crystal structure. The microstructures were observed on an FEI Verios 460 L field emission scanning electron microscope (SEM), high-resolution transmission electronic microscope (HRTEM) with FEG (Talos F200X), and a high-angle annular dark field scanning transmission electronic microscope (Titan Themis Cubed G2 60–300) equipped with an Oxford SDD X-Max energy dispersive X-ray spectrometer (EDS). The chemical valences and surface compositions were analyzed with a THERMO SCIENTIFIC ESCALAB 250xi X-ray photoelectronic spectrometer (XPS), using monochromatized Al_{Kα} X-ray as the excitation source, and C 1s (284.80 eV) as the reference line.

The XAFS spectra at the Au L₃ ($E_0 = 11\,919.0$ eV) edge were measured at the BL14W1 beamline of the Shanghai Synchrotron Radiation Facility (SSRF) operated at 3.5 GeV under “top-up” mode with a constant current of 260 mA. The XAFS data were recorded under transmission mode with two Oxford ion chambers. The energy was calibrated according to the absorption edge of pure Au foil. Athena and Artemis codes were used to extract the data and fit the profiles. For the X-ray absorption near edge structure (XANES) part, the experimental absorption coefficients as function of energies $\mu(E)$ were processed by background subtraction and normalization procedures, and reported as “normalized absorption” with $E_0 = 11\,919.0$ eV for the measured sample and Au foil standard. For the extended X-ray absorption fine structure (EXAFS) part, the Fourier transformed (FT) data in R space were analyzed by applying the first-shell approximate model for Au-Cu contributions, and metallic Au model for Au-Au contributions. The passive electron factors, S_0^2 , were determined by fitting the experimental data on Au foils and fixing the coordination number (CN) of Au-Au to 12, and then fixed for further analysis of the tested samples. The parameters describing the electronic properties (e.g., correction to the photoelectron energy origin, E_0) and local structure environment including CN , bond distance (R), and Debye-Waller factor around the absorbing atoms were allowed to vary during the fitting process. The fitted ranges for k and R spaces were selected to be $k = 3\text{--}12 \text{ \AA}^{-1}$ with $R = 1.0\text{--}3.5 \text{ \AA}$ (k^3 weighted).

Electrochemical measurements

A three-electrode system was used with the self-supported nanoporous Au₃Cu alloy as the working electrode and Pt as the counter electrode on an electrochemical station (CHI 760E). All the potentials were measured against an Ag/AgCl reference electrode (3.0 M KCl), and converted to the RHE reference scale using the equation E (vs. RHE) = E (vs. Ag/AgCl) + 0.1989 V + 0.0591 V × pH. The CO₂ RR was used to probe the electrocatalytic performance over nanoporous electrodes (Figure S1). Nanoporous Cu was evaluated on carbon paper because of its powder form. The tests were performed in a two-compartment electrochemical cell with a piece of anion exchange membrane (Nafion 117) as the separator. The electrolyte was 0.1 M KHCO₃ saturated with CO₂ at a pH value of 6.8. Each compartment contained 40 mL electrolyte. Before the reaction was initiated, the electrolyte in the cathodic compartment was bubbled with CO₂ gas for at least 30 min. Magnetic stirring was applied at a rate of 500 rpm throughout the tests.

CO₂ RR product analysis

CO₂ gas was bubbled into the cathodic compartment at an average rate of 10 sccm (at room temperature and ambient pressure), and was vented directly into the gas sampling loop of a gas chromatograph (GC9790II, Zhejiang Fuli Analyzing Instruments Co. Ltd.). The GC was initiated every 25 min, and nitrogen (99.999%) was used as the carrier gas. The separated gas mixtures were passed through a thermal conductivity detector (TCD), with which the concentration of hydrogen was analyzed. The concentration of CO was analyzed by using a flame ionization detector (FID) with a methanizer.

Theoretical calculations

All the calculations in this work were performed using the Generalized gradient approximation (GGA)-Perdew, Burke and Ernzerhof (PBE)^[24] in the full-electron DMol³ program.^[25] The normal metal surfaces were simulated using the (111) surface of Cu, Au, and Au₃Cu alloy with a five-layered slab of (4 × 4) surface unit cell. The (311) surface was simulated over porous Au₃Cu and Au with a five-layered slab of (3 × 3) surface unit cell. There was a vacuum region of 30 Å between repeated slabs. In our calculations, the atoms in the bottom two layers were fixed at their bulk position and those in the top three layers together with the adsorbates were allowed to relax. The double numerical plus polarization (DNP) basis set was used throughout the calculations. The convergence criteria were set to be 1×10^{-5} Ha, 0.001 Ha Å⁻¹, and 0.005 Å for energy, force, and displacement convergence, respectively. A self-consistent field (SCF) density convergence with a threshold value of 1×10^{-6} Ha was specified. K-points were sampled using the 3 × 3 × 1 Monkhorst-Pack mesh. The Gibbs free energy diagrams for CO₂ reduction were calculated with reference to the computational hydrogen electrode (CHE) proposed by Nørskov et al.^[26] A vibrational analysis was used to calculate the thermodynamic properties of all related molecules in the gas phase and stable adsorption state involved in the reaction.

The formation free energy for *COOH and adsorption free energy for *CO were calculated according to Equations (1) and (2), respectively.

$$\Delta G_{\text{COOH}} = G_{\text{COOH}^*} - (G_* + G_{\text{CO}_2} + \frac{1}{2}G_{\text{H}_2}) \quad (1)$$

$$\Delta G_{\text{CO}} = G_{\text{CO}^*} - (G_* + G_{\text{CO}}) \quad (2)$$

Acknowledgements

The authors gratefully acknowledge financial support from the National Natural Science Foundation of China (21771137, 21773288), the Key Project of Natural Science Foundation of Tianjin (Contract No.18JCZDJC97200), and the Training Project of Innovation Team of Colleges and Universities in Tianjin (TD13-5020). We acknowledge the National Supercomputing Center in Shenzhen for providing the computational resources and materials studio (version 7.0, DMol³).

Conflict of interest

The authors declare no conflict of interest.

Keywords: alloys · AuCu · carbon dioxide reduction · electrocatalysis · electrochemistry · nanoporous alloys · self-supported

- [1] a) T. Zheng, K. Jiang, H. Wang, *Adv. Mater.* **2018**, *30*, 1802066; b) D. U. Nielsen, X.-M. Hu, K. Daasbjerg, T. Skrydstrup, *Nat. Catal.* **2018**, *1*, 244–254; c) A. D. Handoko, F. Wei, Jennndy, B. S. Yeo, Z. W. Seh, *Nat. Catal.* **2018**, *1*, 922–934.
- [2] a) X. Duan, J. Xu, Z. Wei, J. Ma, S. Guo, S. Wang, H. Liu, S. Dou, *Adv. Mater.* **2017**, *29*, 1701784; b) F. Zhao, Q. Yuan, B. Luo, C. Li, F. Yang, X. Yang, Z. Zhou, *Sci. China Mater.* **2019**, *62*, 1877–1887.
- [3] Z. Huang, X. Gu, Q. Cao, P. Hu, J. Hao, J. Li, X. Tang, *Angew. Chem. Int. Ed.* **2012**, *51*, 4198–4203; *Angew. Chem.* **2012**, *124*, 4274–4279.
- [4] a) J. Wu, T. Sharifi, Y. Gao, T. Zhang, P. M. Ajayan, *Adv. Mater.* **2019**, *31*, 1804257; b) M. König, J. Vaes, E. Klemm, D. Pant, *iScience* **2019**, *19*, 135–160.
- [5] a) D. Kim, J. Resasco, Y. Yu, A. M. Asiri, P. Yang, *Nat. Commun.* **2014**, *5*, 4948; b) D. Kim, C. Xie, N. Becknell, Y. Yu, M. Karamad, K. Chan, E. J. Crumlin, J. K. Nørskov, P. Yang, *J. Am. Chem. Soc.* **2017**, *139*, 8329–8336.
- [6] Z. Weng, X. Zhang, Y. Wu, S. Huo, J. Jiang, W. Liu, G. He, Y. Liang, H. Wang, *Angew. Chem. Int. Ed.* **2017**, *56*, 13135–13139; *Angew. Chem.* **2017**, *129*, 13315–13319.
- [7] M. F. Alqahtani, K. P. Katuri, S. Bajracharya, Y. Yu, Z. Lai, P. E. Saikaly, *Adv. Funct. Mater.* **2018**, *28*, 1804860.
- [8] a) S. Zhao, R. Jin, R. Jin, *ACS Energy Lett.* **2018**, *3*, 452–462; b) S. Cai, R. Wang, W. M. Yourey, J. Li, H. Zhang, H. Tang, *Sci. Bull.* **2019**, *64*, 968–975.
- [9] a) D. Gao, R. M. Arán-Ais, H. S. Jeon, B. Roldan Cuenya, *Nat. Catal.* **2019**, *2*, 198–210; b) X. Yuan, L. Zhang, L. Li, H. Dong, S. Chen, W. Zhu, C. Hu, W. Deng, Z. J. Zhao, J. Gong, *J. Am. Chem. Soc.* **2019**, *141*, 4791–4794.
- [10] a) Q. Lu, J. Rosen, Y. Zhou, G. S. Hutchings, Y. C. Kimmel, J. G. Chen, F. Jiao, *Nat. Commun.* **2014**, *5*, 3242–3248; b) F. Li, L. Chen, G. P. Knowles, D. R. MacFarlane, J. Zhang, *Angew. Chem. Int. Ed.* **2017**, *56*, 505–509; *Angew. Chem.* **2017**, *129*, 520–524.
- [11] S. M. Lee, H. Lee, J. Kim, S. H. Ahn, S. T. Chang, *Appl. Catal. B* **2019**, *259*, 118045.
- [12] a) E. L. Clark, C. Hahn, T. F. Jaramillo, A. T. Bell, *J. Am. Chem. Soc.* **2017**, *139*, 15848–15857; b) D. Ren, Y. Deng, A. D. Handoko, C. S. Chen, S. Mal-khandi, B. S. Yeo, *ACS Catal.* **2015**, *5*, 2814–2821.
- [13] W. Zhang, J. He, S. Liu, W. Niu, P. Liu, Y. Zhao, F. Pang, W. Xi, M. Chen, W. Zhang, S. S. Pang, Y. Ding, *Nanoscale* **2018**, *10*, 8372–8376.
- [14] a) Y. Wang, P. Han, X. Lv, L. Zhang, G. Zheng, *Joule* **2018**, *2*, 2551–2582; b) Y. Li, F. Cui, M. B. Ross, D. Kim, Y. Sun, P. Yang, *Nano Lett.* **2017**, *17*, 1312–1317; c) T. T. H. Hoang, S. Verma, S. Ma, T. T. Fister, J. Timoshenko, A. I. Frenkel, P. J. A. Kenis, A. A. Gewirth, *J. Am. Chem. Soc.* **2018**, *140*, 5791–5797; d) T.-T. Zhuang, Z.-Q. Liang, A. Seifitokaldani, Y. Li, P. De Luna, T. Burdyny, F. Che, F. Meng, Y. Min, R. Quintero-Bermudez, C. T. Dinh, Y. Pang, M. Zhong, B. Zhang, J. Li, P.-N. Chen, X.-L. Zheng, H. Liang, W.-N. Ge, B.-J. Ye, D. Sinton, S.-H. Yu, E. H. Sargent, *Nat. Catal.* **2018**, *1*, 421–428; e) J. J. Lv, M. Jouny, W. Luc, W. Zhu, J. J. Zhu, F. Jiao, *Adv. Mater.* **2018**, *30*, 1803111; f) T.-T. Zhuang, Y. Pang, Z.-Q. Liang, Z. Wang, Y. Li, C.-S. Tan, J. Li, C. T. Dinh, P. De Luna, P.-L. Hsieh, T. Burdyny, H.-H. Li, M. Liu, Y. Wang, F. Li, A. Proppe, A. Johnston, D.-H. Nam, Z.-Y. Wu, Y.-R. Zheng, A. H. Ip, H. Tan, L.-J. Chen, S.-H. Yu, S. O. Kelley, D. Sinton, E. H. Sargent, *Nat. Catal.* **2018**, *1*, 946–951; g) P. De Luna, R. Quintero-Bermudez, C.-T. Dinh, M. B. Ross, O. S. Bushuyev, P. Todorović, T. Regier, S. O. Kelley, P. Yang, E. H. Sargent, *Nat. Catal.* **2018**, *1*, 103–110.
- [15] a) H. Xie, T. Wang, J. Liang, Q. Li, S. Sun, *Nano Today* **2018**, *21*, 41–54; b) X. Li, H. J. Qiu, J. Q. Wang, Y. Wang, *Corros. Sci.* **2016**, *106*, 55–60; c) P. Strasser, S. Kühl, *Nano Energy* **2016**, *29*, 166–177; d) L. Lu, X. Sun, J. Ma, D. Yang, H. Wu, B. Zhang, J. Zhang, B. Han, *Angew. Chem. Int. Ed.* **2018**, *57*, 14149–14153; *Angew. Chem.* **2018**, *130*, 14345–14349.
- [16] a) T. Fujita, P. Guan, K. McKenna, X. Lang, A. Hirata, L. Zhang, T. Tokunaga, S. Arai, Y. Yamamoto, N. Tanaka, Y. Ishikawa, N. Asao, Y. Yamamoto, J. Erlebacher, M. Chen, *Nat. Mater.* **2012**, *11*, 775–780; b) P. Liu, P. Guan, A. Hirata, L. Zhang, L. Chen, Y. Wen, Y. Ding, T. Fujita, J. Erlebacher, M. Chen, *Adv. Mater.* **2016**, *28*, 1753–1759.
- [17] a) J. Wen, K. Wu, D. Yang, J. Tian, Z. Huang, A. S. Filatov, A. Lei, X.-M. Lin, *ACS Appl. Mater. Interfaces* **2018**, *10*, 25930–25935; b) W. Luo, W. Xie, R. Mutschler, E. Oveisi, G. L. De Gregorio, R. Buonsanti, A. Züttel, *ACS Catal.* **2018**, *8*, 6571–6581; c) Y. Lum, J. W. Ager, *Angew. Chem. Int. Ed.* **2018**, *57*, 551–554; *Angew. Chem.* **2018**, *130*, 560–563.
- [18] a) T. Bligaard, J. K. Nørskov, *Electrochim. Acta* **2007**, *52*, 5512–5516; b) H. Wang, S. Yin, Y. Xu, X. Li, A. A. Alshehri, Y. Yamauchi, H. Xue, Y. V. Kaneti, L. Wang, *J. Mater. Chem. A* **2018**, *6*, 8662–8668; c) C. Du, M. Chen, W. Wang, Q. Tan, K. Xiong, G. Yin, *J. Power Sources* **2013**, *240*, 630–635.
- [19] J. P. Perdew, K. Burke, M. Ernzerhof, *Phys. Rev. Lett.* **1996**, *77*, 3865–3868.
- [20] M. Kuhn, T. K. Sham, *Phys. Rev. B Condens Matter.* **1994**, *49*, 1647–1661.
- [21] J. C. Bauer, D. Mullins, M. Li, Z. Wu, E. A. Payzant, S. H. Overbury, S. Dai, *Phys. Chem. Chem. Phys.* **2011**, *13*, 2571–2581.
- [22] a) H. Mistry, R. Reske, P. Strasser, B. R. Cuenya, *Catal. Today* **2017**, *288*, 30–36; b) Z. Tao, Z. Wu, X. Yuan, Y. Wu, H. Wang, *ACS Catal.* **2019**, *9*, 10894–10898; c) W. Zhu, K. Zhao, S. Liu, M. Liu, F. Peng, P. An, B. Qin, H. Zhou, H. Li, Z. He, *J. Energy Chem.* **2019**, *37*, 176–182.
- [23] X. Nie, M. R. Esopi, M. J. Janik, A. Asthagiri, *Angew. Chem. Int. Ed.* **2013**, *52*, 2459–2462; *Angew. Chem.* **2013**, *125*, 2519–2522.
- [24] J. K. Nørskov, J. Rossmeisl, A. Logadottir, L. Lindqvist, *J. Phys. Chem. B* **2004**, *108*, 17886–17892.
- [25] a) B. Delley, *J. Chem. Phys.* **1990**, *92*, 508–517; b) B. Delley, *J. Chem. Phys.* **2000**, *113*, 7756–7764.
- [26] A. I. Frenkel, C. W. Hills, R. G. Nuzzo, *J. Phys. Chem. B* **2001**, *105*, 12689–12703.

Manuscript received: October 9, 2019

Accepted manuscript online: December 4, 2019

Version of record online: January 21, 2020